



Half-unit-cell ZnIn_2S_4 monolayer with sulfur vacancies for photocatalytic hydrogen evolution



Chun Du^a, Qian Zhang^b, Zhaoyong Lin^a, Bo Yan^a, Congxin Xia^b, Guowei Yang^{a,*}

^a State Key Laboratory of Optoelectronic Materials and Technologies, Nanotechnology Research Center, School of Materials Science & Engineering, Sun Yat-sen University, Guangzhou, 510275, Guangdong, China

^b College of Physics and Materials Science, Henan Normal University, Xinxiang, Henan, 453007, China

ARTICLE INFO

Keywords:

Half-unit-cell ZnIn_2S_4 monolayer
Carrier lifetime
Photocatalytic hydrogen evolution

ABSTRACT

Two-dimensional (2D) photocatalytic materials have attracted extensive attention due to the unique properties different from those of their bulk. 2D ZnIn_2S_4 nanosheets with the intrinsic bilayer in one-unit-cell with interlayer force generally perform better than that of the bulk in photocatalytic hydrogen evolution. Here, we for the first time demonstrate that the half-unit-cell ZnIn_2S_4 monolayer possesses an excellent photocatalytic performance compared with the one-unit-cell bilayer owing to its increased carrier lifetime. Meanwhile, sulfur vacancies are introduced in the half-unit-cell ZnIn_2S_4 monolayer to trap the photo-generated electrons and further prolong the carrier lifetime. First-principle calculations reveal that sulfur vacancies in the ZnIn_2S_4 monolayer induce more charge carriers at the valence band maximum to participate in the photocatalytic activity. As expected, the photocatalytic hydrogen production rate of the monolayer ZnIn_2S_4 with sulfur vacancies is up to 13.478 mmol/g/h under the visible light irradiation, which is much higher than the available values reported of ZnIn_2S_4 so far. These findings provide a new strategy for optimization of 2D photocatalysts to enhance photocatalytic hydrogen evolution.

1. Introduction

Photocatalytic hydrogen evolution through water splitting, as an important potential method for clean energy production by utilizing solar energy directly, has received much attention [1–3]. However, improving the photocatalytic efficiency is still a great challenge in practical applications [1]. Fortunately, the discovery of 2D materials has opened up one effective approach to enhance photocatalytic performance owing to their unique properties including high specific surface areas, better charge-carrier separation rate, and abundant surface active sites [4,5]. Among various 2D semiconductor materials, ZnIn_2S_4 is attracting dramatically increasing interest due to its visible-light absorption, photo-stability and suitable energy band gap structure for hydrogen evolution reaction (HER) [6,7]. To date, few-layer ZnIn_2S_4 nanosheets have been produced because of the intrinsic bilayer structure in one-unit-cell with interlayer force, and they generally exhibits better than that of the bulk in photocatalytic hydrogen production performance. Actually, there is another 2D ZnIn_2S_4 , i.e., the half-unit-cell ZnIn_2S_4 monolayer, but it has rarely been investigated [8,9].

Benefiting from the peculiar electronic structures, monolayer materials exhibit different properties compared with the few-layer

materials such as WS_2 , WSe_2 , BN, and MoS_2 [10–13]. In particular, monolayer graphene has been applied in various fields due to the larger specific surface area, higher electron mobility and thermal conductivity [14–16]. As for 2D photocatalyst, it can readily shorten the diffusion distance of charge carriers with the reduction in the thickness, which can greatly prolong the lifetime of photo-generated charge carriers [17]. From this perspective, 2D monolayer should have a great prospect in photocatalysis. Nonetheless, there have no any studies about the comparison of photocatalytic performance between the half-unit-cell ZnIn_2S_4 monolayer and the unit-cell ZnIn_2S_4 bilayer. Therefore, the half-unit-cell ZnIn_2S_4 monolayer should be desired to exploit as an advanced photocatalyst.

On the other hand, vacancy engineering has been considered as an effective strategy to improve photocatalytic efficiency in the recent years. For instance, oxygen vacancies in ultrathin In_2O_3 sheets could enhance the absorption of visible light through narrowing the band gap by appearance of a defect level. Further, it can trap the photo-generated electrons to effectively suppress the recombination of carrier, and thus enhancing the water splitting performance [18]. Similar phenomena are also observed in ZnS with sulfur vacancies, Bi_2WO_6 and SrTiO_3 with oxygen vacancies [19–21]. Inspired by these researches, sulfur

* Corresponding author.

E-mail address: stsyygw@mail.sysu.edu.cn (G. Yang).

vacancies should be designed in the ZnIn_2S_4 monolayer to improve the HER performance.

Herein, the one-unit-cell bilayer and half-unit-cell ZnIn_2S_4 monolayer were synthesized using a hydrothermal method with different solvents. Compared with the one-unit-cell ZnIn_2S_4 bilayer, the half-unit-cell ZnIn_2S_4 monolayer exhibits better photocatalytic hydrogen evolution due to the shorter diffusion length which effectively inhibits the recombination of photo-generated electron-hole pairs. Interestingly, excess thioacetamide can be adsorbed on the surface of the primary nanocrystal, which can partially hinder the growth of crystal and lead to the formation of the structure with vacancies [22,23]. Therefore, sulfur vacancies were introduced in the half-unit-cell ZnIn_2S_4 monolayer to trap the photo-generated electrons and prolong the carrier lifetime. Intriguingly, the ZnIn_2S_4 monolayer with sulfur vacancies exhibits a high photocatalytic hydrogen production rate up to 13.478 mmol/g/h under the visible light irradiation, which is approximately 16.9 and 7.8 times higher than that of ZnIn_2S_4 bilayer and monolayer, respectively, due to longer carrier lifetime and the unique electronic structure, which is supported by the characterizations and the first-principles calculations. These findings provide a new perspective to design photocatalyst with lamellar structure for accessing efficient photocatalytic hydrogen production.

2. Experimental

2.1. Materials

$\text{Zn}(\text{CH}_3\text{COO})_2 \cdot 2\text{H}_2\text{O}$ (99.8%), InCl_3 (99.8%), thioacetamide (TAA, 99.8%), triethanolamine (TEOA, 98%) were obtained from Alfa Aesar. Polyvinylidene fluoride (PVDF, AR), 1-methyl-2-pyrrolidinone (NMP, 99%), 3',5,5'-tetramethyl-benzidine (TMB, 99%) and peroxidase (POD, 300 u/mg) were purchased from Aladdin Industrial Corporation. Absolute ethanol and NaSO_4 (99%) were purchased from Guangzhou Chemical Reagent Factory. All the materials were used without further purification. Deionized water ($18.2 \text{ M}\Omega \text{ cm}^{-1}$) was used throughout the experiments.

2.2. Synthesis of ZnIn_2S_4 bilayer

To synthesize the ZnIn_2S_4 bilayer, 0.4 mmol $\text{Zn}(\text{CH}_3\text{COO})_2 \cdot 2\text{H}_2\text{O}$, 0.8 mmol InCl_3 and 1.6 mmol TAA were dissolved in 30 ml deionized water with vigorous stirring for 30 min. Then, the mixture was transferred into a 50 ml Teflon-lined autoclave and heated at 180 °C for 24 h. After cooling down to room temperature, the obtained products, labeled as B-ZIS, were collected by centrifugation, washed several times with deionized water and ethanol, and dried at 80 °C in air.

2.3. Synthesis of ZnIn_2S_4 monolayer

The procedure of the ZnIn_2S_4 monolayer is similar to that of the ZnIn_2S_4 bilayer except that all the raw materials were dissolved 15 ml deionized water and 15 ml absolute ethanol. And it was designated as M-ZIS.

2.4. Synthesis of ZnIn_2S_4 monolayer with sulfur vacancies

The procedure of the ZnIn_2S_4 monolayer with sulfur vacancies is similar to that of the ZnIn_2S_4 monolayer except that the raw material TAA was added in solution at 3.2 mmol, and then the obtained product was designated as M-ZIS-S.

2.5. Characterizations

The structures of the as-prepared powders were analyzed on a Rigaku D/Max-IIIA X-ray diffractometer detector with $\text{Cu K}\alpha$ radiation ($\lambda = 1.5406 \text{ \AA}$, 40 kV, 20 mA) at scanning speed of 5° min^{-1} in the 20

range of 10–80°. The detailed microstructures were observed using transmission electron microscopy (TEM, FEI Tecnai G2 F30). The surface morphology and thickness profile were acquired on a Bruker Multimode 8 atomic force microscope (AFM) operated at the tapping mode. The Raman spectra were recorded by an inVia Raman Microscope (Renishaw, England) with a He-Ne laser with a wavelength of 514 nm and maximum output power of 6 mW. The binding energies of Zn, In, S and valence band (VB) were acquired using an ESCALAB 250 X-ray photoelectron spectrometer (XPS, Thermo Fisher Scientific). All of the binding energies were calibrated to the C 1 s peak of adventitious surface carbon at 284.8 eV. The electron spin resonance spectra (ESR) were recorded on a Bruker A300 EPR spectrometer at 300 K and 9.86 GHz. The amount of Zn, In and S in M-ZIS and M-ZIS-S were measured by inductively coupled plasma mass spectrometry (ICP-MS). The UV-vis diffuse reflection spectra (UV-vis DRS) were acquired using a Shimadzu UV-3600 spectrophotometer. The photo-luminescence (PL) spectra (excited by 470 nm light) and time-resolved photoluminescence spectroscopy (TRPL) under the excitation of a hydrogen flash lamp with the wavelength at 406.2 nm (nF900, Edinburgh Instruments) were obtained using a FLSP920 fluorescence lifetime spectrophotometer. The Zeta potentials were determined by EliteSizer Nanoparticle size-Zeta potential and molecular weight analyzer. The specific surface area was determined by the Brunauer-Emmett-Teller (BET) method using a Micromeritics ASAP 2020 M system. Electrochemical measurements were performed on a CHI660E electrochemistry workstation at room temperature. All the measurements were carried out in Na_2SO_4 (0.5 M, PH = 6.8) solution and conducted in a conventional three-electrode cell by using Ag/AgCl (sat. KCl) electrode as the reference electrode, a graphite sheet as the counter electrode and the sample on the fluoride tin oxide (FTO) with an active area of $1.0 \times 1.0 \text{ cm}^2$ as the working electrode. The working electrode was prepared as follows: 1 mg of the sample, 20 μl 5 mg/ml PVDF solution and 20 μl NMP were mixed by ultrasonic oscillation to obtain a suspension, which was then coated onto the FTO glass substrate. Finally, the coated FTO glass was dried at 60 °C to obtain the working electrode.

2.6. Photocatalytic hydrogen (H_2) evolution activity

The photocatalytic H_2 evolution activity was carried out in a 250 ml Pyrex top-irradiation photo-reactor connected to a closed gas-circulation system using a 300 W Xe lamp equipped with a 400 nm cut-off filter at 5 °C. The light power density is 80 mW/cm^2 . 20 mg photocatalyst was dispersed in 100 ml aqueous solution containing 10 ml TEOA as sacrificial reagents in a Pyrex flask. After a 30 min degassing pretreatment, the suspension was irradiated for 5 h and the amount of H_2 was analyzed using a on-line gas chromatograph (SP7800, TCD, molecular sieve 5 A , N_2 carrier, Beijing Keruida Limited). To evaluate the H_2 evolution stability, the photocatalyst was reused for four times. And the quantum efficiency (QE) was detected under irradiation for 5 h with various band-pass filter including 365, 405, 420, 500, 580, and 670 nm which the average intensity of irradiation were 2.51, 6.45, 4.93, 5.32, 4.03 and 7.13 mW/cm^2 , respectively.

2.7. Hydrogen peroxide (H_2O_2) detection experiment

The photo-produced H_2O_2 was detected by UV-vis spectroscopy using TMB as the peroxide indicator. Herein, 0.2 mg photocatalyst was added into 2 ml aqueous solution containing 6.25 u/ml POD and 500 umol/ml TMB in the dark. Then, the color changed to blue by irradiation for 10 min using a 300 W Xe lamp with a 400 nm cut-off filter under vacuum. After centrifugation, the reaction supernatant was collected to measure the absorbance of the presence of H_2O_2 at a characteristic peak wavelength of 652 nm.

2.8. Calculation method

The theoretical simulations are carried out by the Vienna ab initio simulation package (VASP) package based on the density functional theory (DFT) calculations. The Perdew-Burke-Ernzerhof (PBE) within the generalized gradient approximation (GGA) treats the exchange-correlation functional, while the projected augmented wave (PAW) describes the electron-ion interaction. Moreover, the kinetic energy cutoff and k-point meshes are set to be 500 eV and $9 \times 9 \times 1$, respectively. Meanwhile, the convergence criterion of the energy and force within the process of geometric optimization is chosen as 10^{-5} eV and 0.01 eV/Å, respectively. And the vacuum region of 20 Å are applied to eliminate the interaction due to the periodic image in the 2D ZnIn₂S₄ monolayer system.

3. Results and discussion

3.1. Morphology and structure of ZnIn₂S₄ nanosheets

Morphology and structure of the ZnIn₂S₄ bilayer (B-ZIS), the ZnIn₂S₄ monolayer (M-ZIS) and the ZnIn₂S₄ monolayer with S vacancies (M-ZIS-S) samples were systematically characterized. Fig. S1 shows the XRD patterns of B-ZIS, M-ZIS, and M-ZIS-S. The peaks of all the samples are in good agreement with the standard pattern of the hexagonal ZnIn₂S₄ (JCPDS file No. 72-0773), revealing the high purity. And the 2θ diffraction peaks at 21.5°, 27.6°, 30.4°, 39.7°, 47.1°, 52.4°, and 55.5° can be indexed to (006), (102), (104), (108), (110), (116), and (202), respectively. However, the intensity of the diffraction peak of facet (104) of M-ZIS-S becomes weaker due to the reaction with a high concentration of TAA which could inhibit the growth of crystal [23]. It suggests that M-ZIS-S may achieve a defect structure.

As depicted in Fig. 1a–c, TEM images reveal that all the samples have a hexagonal ultrathin structure. Moreover, HRTEM image shows the interplanar crystal spacing of M-ZIS-S is 0.32 nm which can be assigned to the (102) face of ZnIn₂S₄ in Fig. 1d in the region indicated by the red square in Fig. 1c. And the absence of some atoms can be seen clearly in the white circle in Fig. 1e of the false-color image of the HRTEM image, arising from the existence of defects. This observation confirms that M-ZIS-S has a defect structure via solvothermal method with excess TAA which is in line with the XRD results. Furthermore, AFM was carried out to measure the thickness of the samples. The thickness of B-ZIS is about 2.5 nm (Fig. S2a and 2b), indicating that the obtained B-ZIS has two layer structure based on bilayer with a thickness of 2.468 nm along the c axis, while the thickness of M-ZIS nanosheet is about 1.1–1.3 nm (Fig. S2c and 2d). As described in Fig. 1f, M-ZIS-S exhibits a thickness of 1.29 nm and the corresponding height profiles is shown in Fig. 1g. Meanwhile, many nanosheets were measured in Fig. S2e and 2f to obtain the thickness. It suggests that M-ZIS and M-ZIS-S have a monolayer structure.

Furthermore, Raman spectroscopy was carried out to obtain more information about the crystal structure of ZnIn₂S₄. As shown in Fig. 1h, the Raman spectra of all the samples are characterized by three Raman bands around 248, 294, and 358 cm⁻¹, which can be assigned to the longitudinal optical mode (LO₁), transverse optical mode (TO₂), and longitudinal optical mode (LO₂) of ZnIn₂S₄, respectively [24,25]. However, the intensity of Raman peaks in M-ZIS and M-ZIS-S become weaker and broader than that of B-ZIS and the peaks exhibit a slight shift due to the different number of layers according to previous Raman spectral analysis of WS₂ and WSe₂ [10,11]. This analysis is in good agreement with the result of AFM for ZnIn₂S₄. Obviously, compared with M-ZIS, the intensity enhancement in M-ZIS-S is attributed to the present of vacancies[26]. From these results, the graphical representations of B-ZIS, M-ZIS, and M-ZIS-S are shown in Fig. 1i to clearly illustrate the different in morphology.

To further identify the presence of S vacancy of samples, the chemical states of S, Zn and In in M-ZIS and M-ZIS-S were analyzed using

XPS measurements. As depicted in Fig. 2a, the spectrum of S 2p in the samples can be fitted to two peaks which are assigned to divalent sulfide ions (S²⁻) [27]. Compared with M-ZIS (161.60 eV, 162.77 eV), the binding energy and the intensity of S 2p in M-ZIS-S (161.35 eV, 162.52 eV) become smaller and weaker, suggesting that there are S vacancies in the structure due to low-coordination S [28–30]. Meanwhile, the intensity ratio of S 2p in M-ZIS-S and M-ZIS is smaller than that of In 3d and Zn 2p (in Supplementary Table 1), which further explain that S vacancies exist in M-ZIS-S benefiting from the reduction of S content. Similarly, this phenomenon is also observed in the In 3d and Zn 2p spectra of M-ZIS and M-ZIS-S (Fig. 2b and 2c), ascribing to In²⁺ and Zn²⁺, respectively [9]. The binding energies for In 3d_{5/2} and In 3d_{3/2} in M-ZIS-S (444.77 eV, 452.31 eV) are lower than those of M-ZIS (444.91 eV, 452.45 eV), as well as that of Zn 2p. However, compared with M-ZIS (1022.05 eV and 1045.11 eV), two peaks at 1021.86 eV and 1044.92 eV contributing from Zn 2p 3/2 and 2p 1/2 of M-ZIS-S (Fig. 2c) are shifted down for 0.19 eV, which is over that of In, indicating that the loss of S atoms around Zn relative to In [30]. From the above discussion, it can be concluded that ZnIn₂S₄ with S vacancies could be prepared successfully by solvothermal method with excess TAA. Additionally, ICP-MS was employed to accurately analyze the amounts of Zn, In and S in M-ZIS and M-ZIS-S. The atomic ratio of Zn, In and S in M-ZIS is 1: 2.2 : 3.6 and the atomic ratio in M-ZIS-S is 1 : 2.2 : 2.6. From the comparison about the atomic proportions of M-ZIS and M-ZIS-S, it can be identified that the S vacancies exist in M-ZIS-S. Moreover, the ESR spectra were employed to further confirm the existence of S-Vacancy in M-ZIS-S which can provide sensitive and direct information about behaviors of native defects. As shown in Fig. 2d, it's obvious to find that M-ZIS-S exhibits a sharp ESR signal at 3503 G (g-value of 2.007), indicating the existence of S vacancies [19,31,32]. On the contrary, the absence of this resonance signal in B-ZIS and M-ZIS confirms that there is no S Vacancy existing in the control sample. This is consistent with the XPS results. Therefore, all the results further demonstrate that ZnIn₂S₄ has been successfully prepared into monolayer 2D nanosheet with S vacancy.

3.2. UV-vis absorption properties

The UV-vis diffuse reflectance spectra of the as-prepared samples were investigated within the scope of 200–800 nm. As can be seen from Fig. 3a, all the sample have a steep absorption edge located from 410 nm to 570 nm, indicating the photo-response in visible light region. Compared with B-ZIS and M-ZIS, M-ZIS-S exhibits slight red shift absorption due to the existence of S vacancy which can absorb more visible light during the photocatalytic H₂ activity [33]. Meanwhile, the optical band gap (E_g) of ZnIn₂S₄, a direct band gap material [34], can be estimated using the Kubelka-Munk function: $ahv^2 = A(hv - E_g)$. As depicted in Fig. 3b, the intersection of the tangent with the x-axis can give a good approximation of the E_g values of the samples, estimating to be 2.34, 2.39 and 2.31 eV for B-ZIS, M-ZIS and M-ZIS-S, respectively.

3.3. Photocatalytic activity for H₂ production

The photocatalytic H₂ evolution was evaluated under visible-light irradiation ($\lambda \geq 400$ nm) in deionized water with TEOA as a hole sacrificial agent. As illustrated in Fig. 4a, M-ZIS exhibits a higher photocatalytic activity compared with B-ZIS, whereas M-ZIS-S shows a higher photocatalytic H₂ production performance than that of B-ZIS and M-ZIS for 4 h. In order to further examine the photocatalytic activity, the H₂ evolution rate was calculated and shown in Fig. 4b. Clearly, M-ZIS-S has the highest H₂ evolution rate of 13.478 mmol/g/h, which is approximately 7.8 and 16.87 times higher than that of B-ZIS and M-ZIS. Moreover, M-ZIS exhibits an enhanced H₂ evolution rate of 1.723 mmol/g/h, in comparison to that of B-ZIS (0.799 mmol/g/h). Fig. 4c presents the action spectra of the photocatalytic H₂ production rate with the UV-vis absorption spectrum for M-ZIS-S. It can be seen

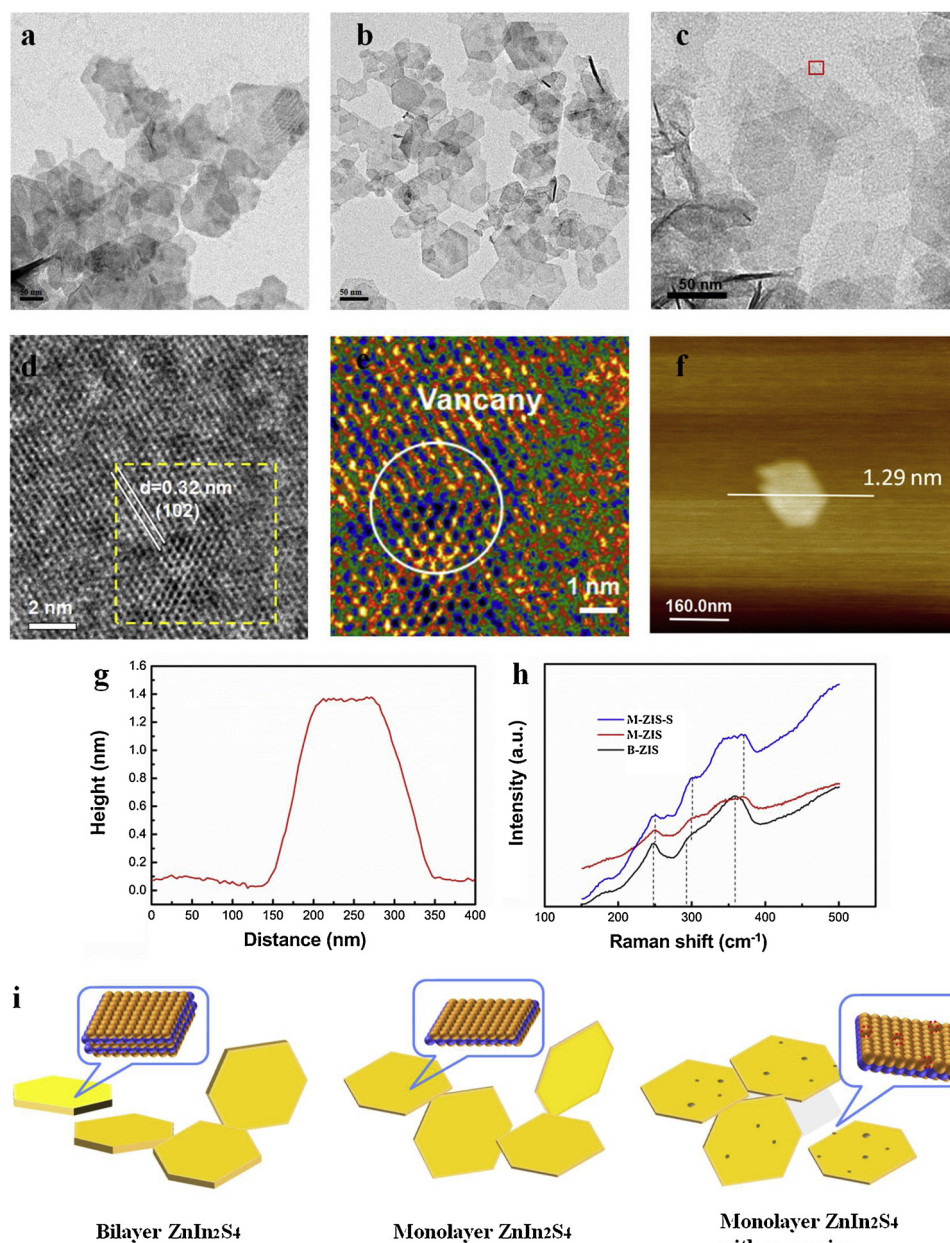


Fig. 1. (a), (b) TEM image of B-ZIS and M-ZIS, respectively, (c) TEM image (d) HRTEM image of the region outlined in red in (c), (e) false-colour image of the HRTEM image of the region outlined in yellow in (d), (f) AFM image, and (g) the corresponding height profiles of M-ZIS-S, (h) Raman spectra and (i) the graphical representations of B-ZIS, M-ZIS and M-ZIS-S (For interpretation of the references to colour in this figure legend, the reader is referred to the web version of this article).

that the variation trend of wavelength-dependent photocatalytic H₂ generation rate is nearly in line with the absorbance spectrum, illustrating that the light response indeed drives the H₂ production. Meanwhile, the QE of M-ZIS-S at different monochromatic light were calculated in Fig.S3. The QE at λ of 365 nm has the highest value up to 53.68% and decreases with increasing wavelength. This result demonstrates that enhancing the light absorption is beneficial to improve the efficiency of solar-to-hydrogen conversion. Besides high hydrogen production rate, stability of photocatalyst is also an important factor for practical application. Therefore, the cycling photocatalytic performance of M-ZIS-S was investigated, shown in Fig. 4d. Obviously, the photocatalytic activity still remains unchanged after 3 cycles and has a little deterioration in the fourth test which might be related to the consumption of the sacrificial reagents. Although the activity for the H₂ evolution exhibits a slight decrease, it still demonstrates the stability of

M-ZIS-S for photocatalytic performance. Additionally, XRD pattern of M-ZIS-S shows no distinct difference between fresh and used sample in Fig. S4. This result further confirms the sufficient stability of M-ZIS-S.

3.4. Optical properties and electrochemical characteristics

Having a good absorption of visible light, M-ZIS-S has a better photocatalytic performance. However, the behavior of light-generated electron-hole pairs is also an important factor to affect performance. Therefore, it is necessary to study the lifetime of photo-generated carriers. PL emission spectra are used to investigate the behavior of light-generated electron-hole pairs in photocatalysts to verify the charge separation effect. In Fig. 5a, among the three samples, B-ZIS shows the strongest emission peak at 554 nm owing to the rapid recombination of electron-hole pairs. In contrast, M-ZIS has a weaker PL peak attributing

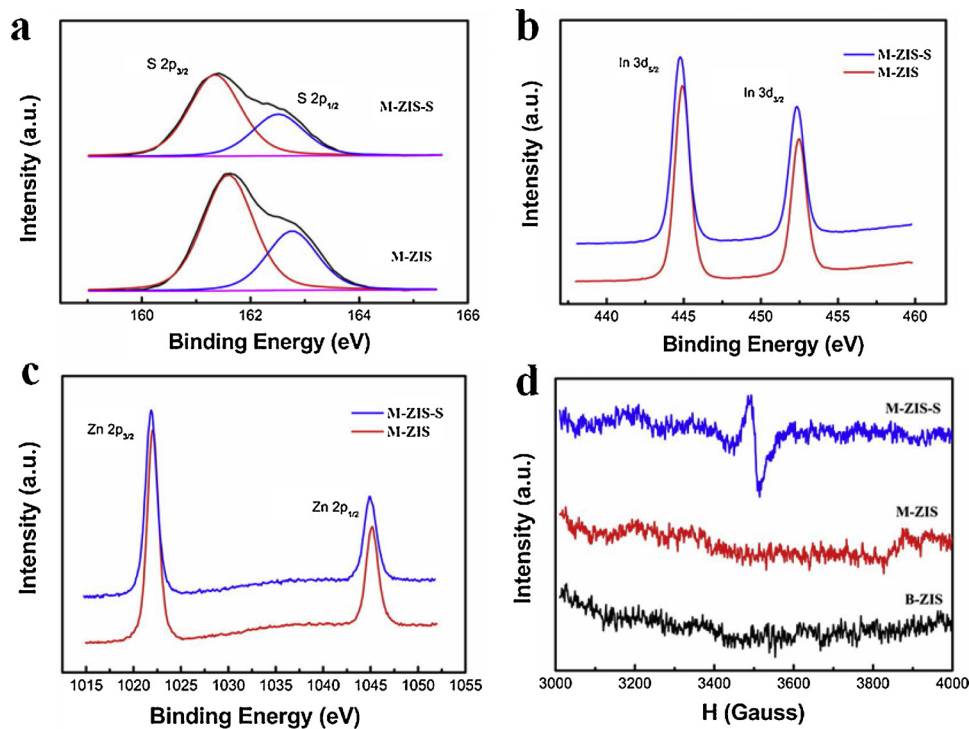


Fig. 2. (a) S 2p, (b) In 3d and (c)Zn 2p XPS spectra of M-ZIS and M-ZIS-S, (d) ESR spectra of B-ZIS, M-ZIS and M-ZIS-S.

to the fast transfer of electrons or holes in the shorter diffusion length in monolayer structure, and there is the weakest PL peak in M-ZIS-S due to the existence of S vacancies. These analyses demonstrate that it's beneficial for electrons or holes to diffuse to the surface with the reduction of thickness, thus effectively inhibiting the recombination of photo-generated electron hole pairs. And then the introduction of S vacancies could trap electrons to separate photo-excited electron-hole pairs for the enhanced photocatalytic performance[35].

Furthermore, TRPL decay spectra are performed to investigate the migration process of photo-induced charge carriers. The average PL lifetime (τ_A) could be calculated according to the equation [36]

$$\tau_A = \frac{A_1 \tau_1^2 + A_2 \tau_2^2}{A_1 \tau_1 + A_2 \tau_2}$$

where τ_1 and τ_2 are the fluorescent lifetime, A_1 and A_2 are the corresponding amplitudes. It's known that the τ_A is related to the short lifetime components (τ_1) and the long lifetime components (τ_2), which are originated from the non-radiative recombination of charge carriers in the surface defect states and ascribed to the interband recombination of the free excitons in the $ZnIn_2S_4$ nanosheets, respectively [37]. As displayed in the inset table of Fig. 5b, the τ_A of M-ZIS is prolonged to

3.23 ns compared with the B-ZIS ($\tau_A = 2.86$ ns), principally attributing to the fast transfer of charge to the surface in the monolayer, which suggest that the electron-hole recombination is dramatically restrained to enhance the photocatalytic activity. As for the M-ZIS-S, the τ_1 (0.542 ns) and τ_2 (5.59 ns) are longer than that of B-ZIS ($\tau_1 = 0.408$ ns, $\tau_2 = 3.41$ ns) and M-ZIS ($\tau_1 = 0.514$ ns, $\tau_2 = 3.79$ ns), mainly deriving from the presence of S vacancies for trapping photo-generated electrons to delay the recombination of electron-hole pairs and the band structure. Apparently, M-ZIS-S has a longer average lifetime ($\tau_A = 5.04$ ns) with respect to B-ZIS ($\tau_A = 2.86$ ns) and M-ZIS($\tau_2 = 3.41$ ns). Benefiting from the existence of S vacancies, the photo-generated electrons on the bottom of conduction band (CB) could be trapped by non-radiative S vacancies and then undergo trap-to-trap hopping for donor-acceptor recombination instead of directly jumping to the valence band (VB) for recombination, leading to the extended carries lifetime [38]. Therefore, M-ZIS-S has good photocatalytic properties that should be ascribed to the much increased lifetime value. This result can be further confirmed by the electrochemical impedance spectroscopy of B-ZIS, M-ZIS, and M-ZIS-S in Fig. 5c. Clearly, the electron-transfer resistance decreases in the order of B-ZIS > M-ZIS > M-ZIS-S, implying that more effective separation of photo-generated electron-hole pair

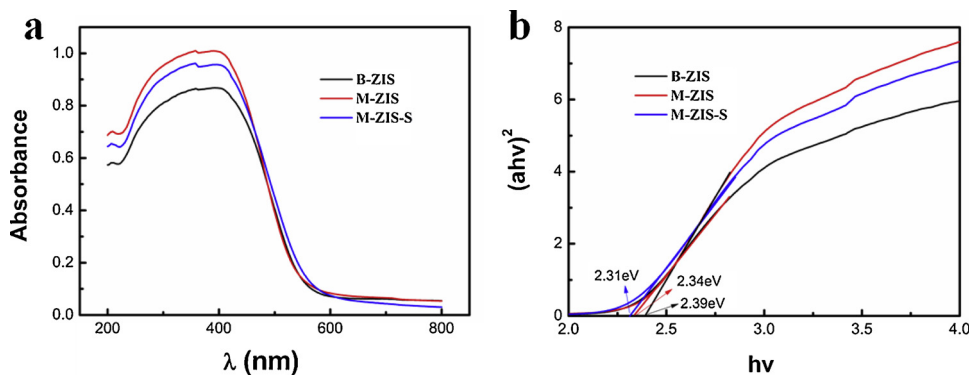


Fig. 3. (a) UV-vis DRS and (b) $(\alpha h\nu)^2$ versus $(h\nu)$ plots of B-ZIS, M-ZIS, and M-ZIS-S.

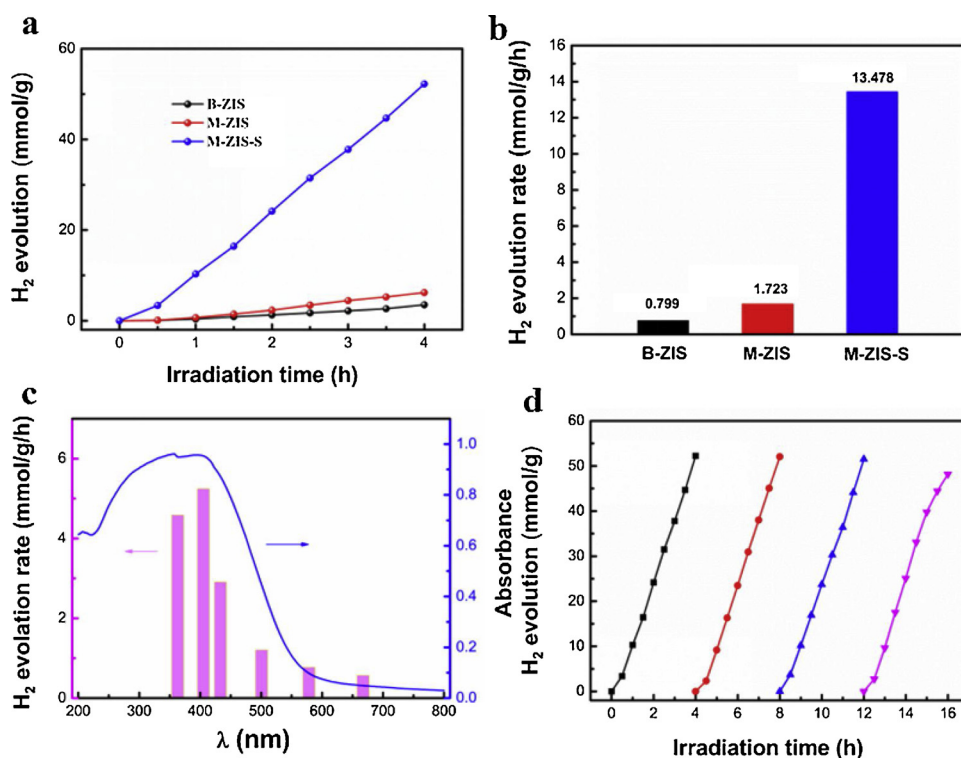


Fig. 4. (a) Photocatalytic H₂ evolution and (b) H₂ evolution rates of B-ZIS, M-ZIS, and M-ZIS-S. (c) Wavelength-dependent H₂ production rate, (d) Recycling photocatalytic test of M-ZIS-S.

transport in M-ZIS-S due to the smaller semicircular part of the Nyquist plots which reflects the charge transfer process. This result is in line with the results of PL and TRPL analyses.

To explore other influences, the surface area of samples were

investigated by BET Nitrogen adsorption–desorption isotherms in Fig.S5. The surface area of M-ZIS ($75.41 \text{ m}^2/\text{g}$) is larger than that of B-ZIS ($61.66 \text{ m}^2/\text{g}$), demonstrating that M-ZIS can expose more surface to participate in reactivity which is beneficial for photocatalysis. As for M-

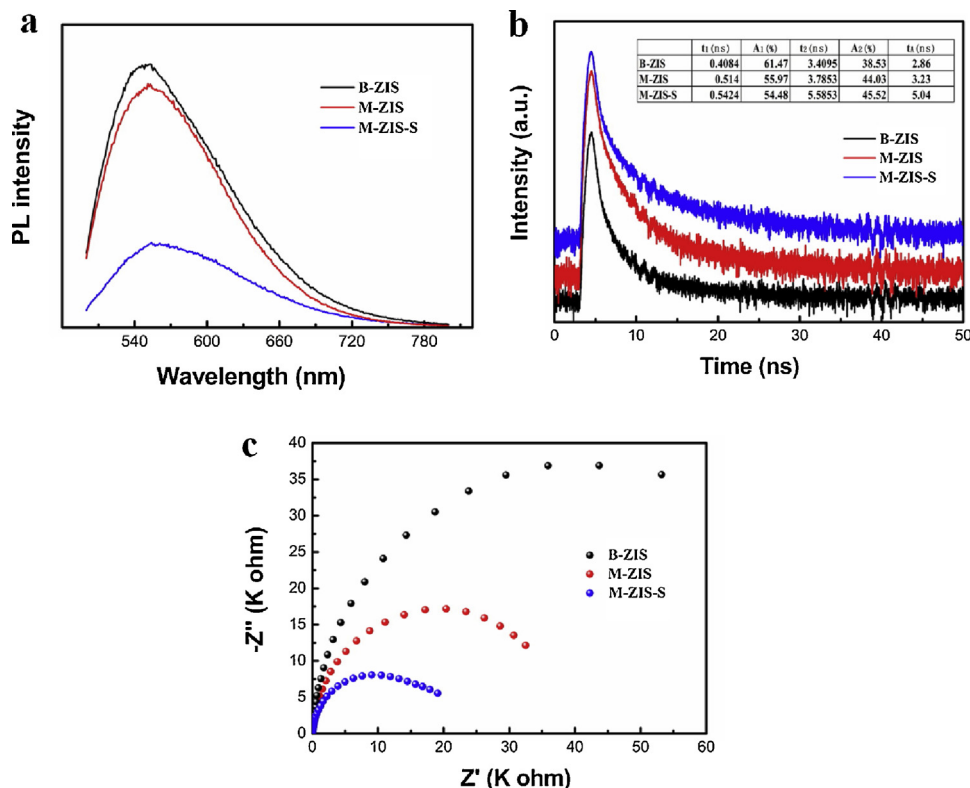


Fig. 5. (a) PL spectra (b) TRPL decay spectra and (c) EIS of B-ZIS, M-ZIS, and M-ZIS-S.

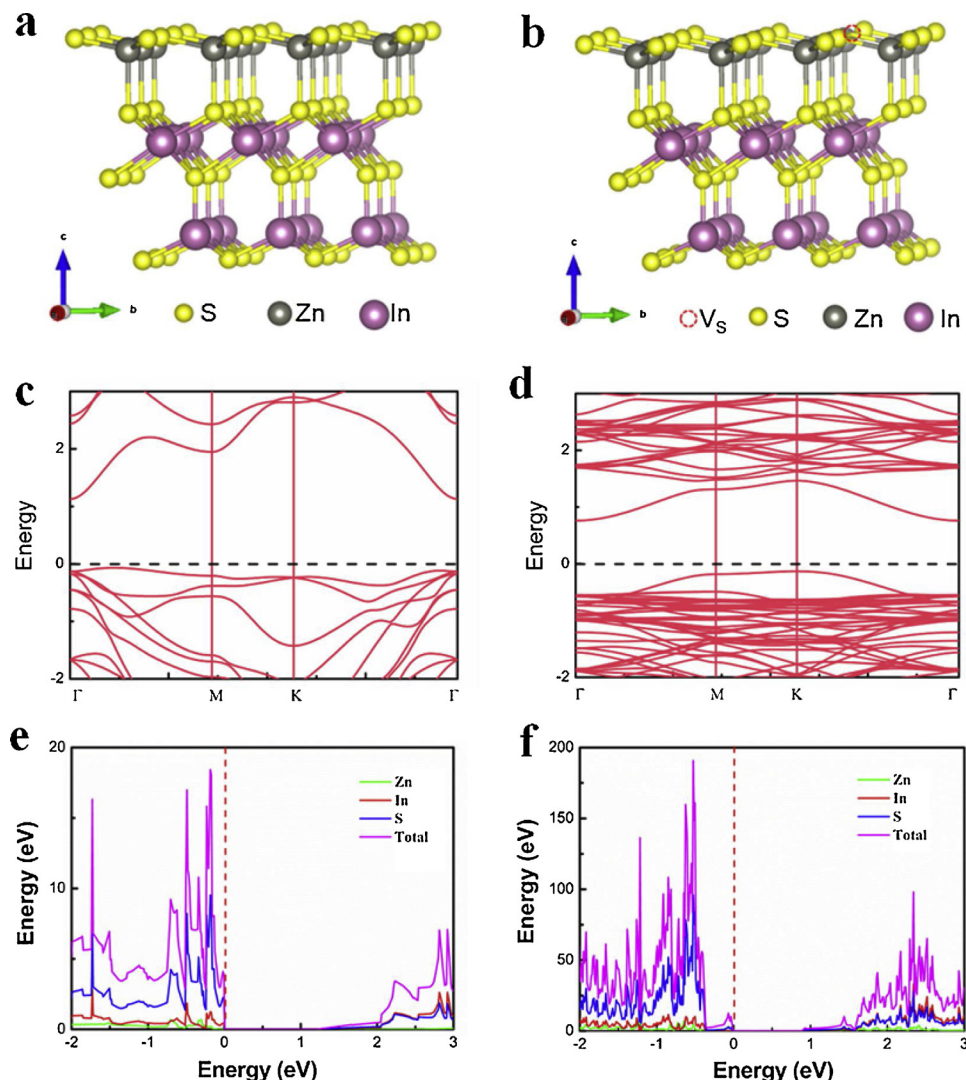


Fig. 6. (a) (b) The geometric structure, (c) (d) band structure, and (e) (f) density of states (DOS) of monolayer ZnIn₂S₄ and monolayer ZnIn₂S₄ with S vacancy, respectively.

ZIS-S, it has the largest surface area ($82.53 \text{ m}^2/\text{g}$) to increase more active reaction sites, leading to the enhanced photocatalytic performance. Furthermore, the linear sweep voltammetry for the as-prepared samples was measured to assess the overpotential which is a criterion to evaluate the HER reaction. A smaller overpotential value for catalyst may indicate that it is easier to produce H₂[39]. As shown in Fig. S6, to reach a current density of $10 \text{ mA}/\text{cm}^2$, an indicator related to solar fuel synthesis [40], the overpotential of M-ZIS is 1.16 eV versus reversible hydrogen electrode (RHE), which is smaller than that of B-ZIS (1.23 eV), while M-ZIS-S has the smallest value (1.14 eV). In addition, Fig. S7 shows that the zeta potential of M-ZIS-S (-39.64 mV) is more negative than that of B-ZIS (-11.35 mV) and M-ZIS (-15.56 mV), indicating that M-ZIS-S can absorb more protons on surface for HER.

3.5. Theoretical calculation

To further investigate the effect of S vacancy in the ZnIn₂S₄ monolayer, the theoretical models are constructed, and we also study their electronic properties used the first-principle calculations within the density functional theory (DFT) framework. The band gap can be obtained from the electronic structure in Fig. 6c and d. Obviously, the band gap of monolayer ZnIn₂S₄ with S vacancy is smaller than the ZnIn₂S₄ monolayer, which is in accordance with the change trend from

the result of UV-vis diffuse reflectance spectra. On top of that, the ZnIn₂S₄ monolayer with S vacancy exhibits a different electronic structure from the ZnIn₂S₄ monolayer ascribing to the contribution by atomic orbitals, which suggests that the electronic properties can be influenced greatly due to the introduction of S vacancy. To further obtain the underlying physical meanings, the density of states (DOS) for the ZnIn₂S₄ monolayer and that with S vacancy are depicted in Fig. 6e and f. It's clearly see that both valence band maximum (VBM) and conduction band minimum (CBM) in the monolayer ZnIn₂S₄ and that with S vacancy are mainly contributed by the S orbital, indicating that S atomic play a dominant role in electronic structure. And the detail information of DOS can be seen in Fig. S8 and S9. For the CBM, both of them are contributed from In-5s5p and S-3p orbital. As for the ZnIn₂S₄ monolayer, the VBM is mainly contributed by the S-3p orbital, whereas the VBM of the ZnIn₂S₄ monolayer with S vacancy is contributed of S-3p and Zn-3p orbital. Moreover, it can be seen that the monolayer ZnIn₂S₄ with S vacancy always exhibits an increased DOS with respect to that of the ZnIn₂S₄ monolayer (Fig. S10), demonstrating that the introduction of S vacancies can affect the electron structure to a large extent, and thus adding more charge carriers, especially at the CBM to participate in the photocatalytic process, which could enhance the photocatalytic performances [41,42].

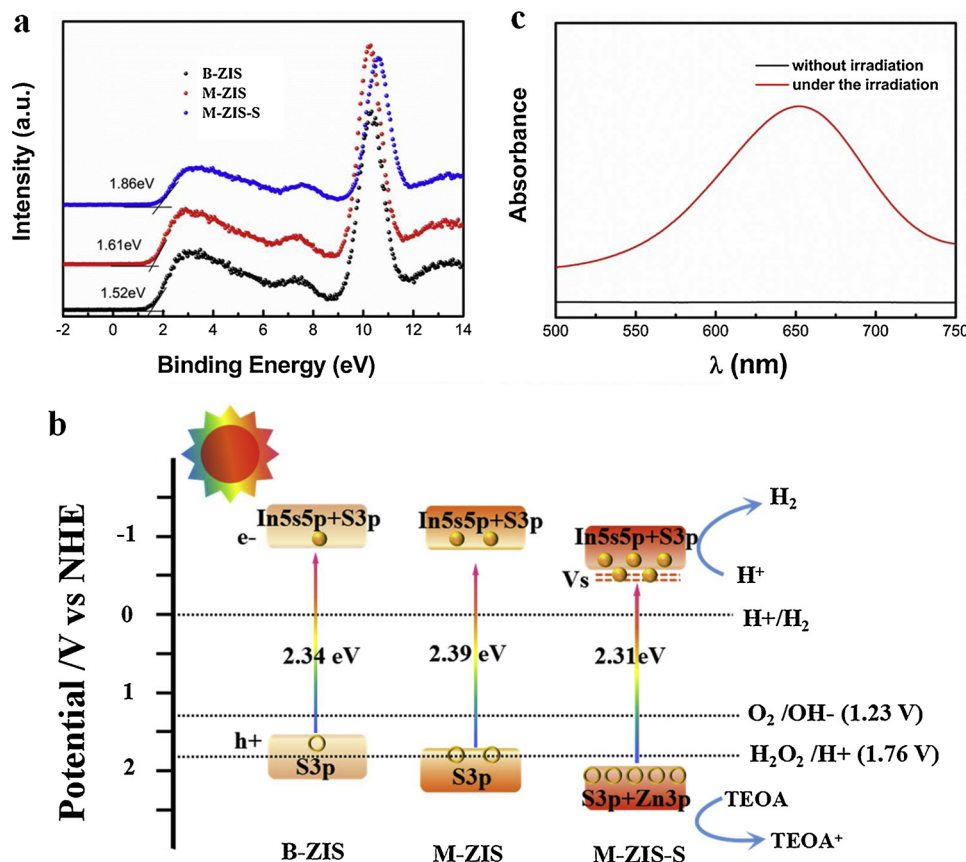


Fig. 7. (a) Valence band XPS (b) a scheme view of the H₂ evolution mechanism for B-ZIS, M-ZIS, and M-ZIS-S (c) typical absorption spectra of the TMB-H₂O₂ mixed solution of M-ZIS-S in the dark and under the irradiation for 10 min ($\lambda \geq 400$ nm).

3.6. Photocatalytic mechanism

As discussed above, M-ZIS has a better photocatalytic performance compared with B-ZIS due to the excellent properties including the elongated lifetime of photo-generated carriers, larger BET and lower overpotential. As for M-ZIS-S, it exhibits the best photocatalytic activity, attributing to the introduction of S vacancies on the basis of a monolayer which can strongly influence the CB to give more charge carries for catalytic reaction. To obtain insight into the photocatalytic mechanism, the VB (E_{VB}) potentials of B-ZIS, M-ZIS, and M-ZIS-S are studied by analyzing the VB XPS spectra and found to be 1.52, 1.61, and 1.86 eV versus the normal hydrogen electrode (NHE), respectively (Fig. 7a). According to the formula $E_{CB} = E_{VB} - E_g$ [43], the CB (E_{CB}) potentials were estimated to be -0.82, -0.78, and -0.45 eV for B-ZIS, M-ZIS, and M-ZIS-S, respectively, based on the values of E_g and E_{VB} . Therefore, a schematic view of the band structures for the samples vs NHE is shown in Fig. 7b. It's found that a reduction in the thickness and the existence of S vacancies in ZnIn₂S₄ contributed to the change of the electronic structure and thus result in the shift of the band potential. Fortunately, the CB potentials of them are still higher than the reduction potentials of H⁺/H₂ [44]. And all the samples are capable of photocatalytic H₂ evolution in spite of the shift of both VB and CB. As for M-ZIS-S, more electrons would transfer from the VB (hybridized S-3p and Zn-3p orbital) to the CB (hybridized In-5s5p and S-3p orbital) during the visible light illumination. Benefiting from the reduction in thickness, photo-induced electrons and holes can migrate to surface for the subsequent reactions effectively. Meanwhile, S vacancies can trap the electrons to suppress the recombination with holes in thermodynamic. After that, the electrons would be reduced by H⁺ to produce H₂ (H⁺ + e⁻ → H₂) and the holes would be consumed by TEOA (TEOA + h⁺ → TEOA⁺). Interestingly, it should be noted that the VB

edge is shift to higher direction compared to the H₂O₂/H⁺ position. Therefore, photo-induced holes could partly react with water to form H₂O₂ (2H₂O + 2h⁺ → H₂O₂ + 2H⁺), enhancing by consuming holes and thus preventing the recombination of charge, as the sacrificial agent does in the photocatalytic process. In order to verify this conjecture, the existence of H₂O₂ was measured by UV-vis spectroscopy using TMB as the peroxide indicator based on the principle that a characteristic peak wavelength at approximately 652 nm indicating the presence of H₂O₂ [45,46]. As shown in Fig. 7c, a significant absorption peak appeared in 652 nm under visible light, demonstrating that H₂O₂ was produced during visible light irradiation. This result further supports that holes could not only be consumed by sacrificial agents, but also react with water for suppressing the recombination of electron and hole efficiently, thus improving the hydrogen production efficiency. That is, M-ZIS-S has a better photocatalytic property ascribing that more electron are photo-excited to transport toward surface and the holes can be simultaneously consumed by dual pathways, boosting the utilization rate of electrons.

4. Conclusion

In summary, one-unit-cell ZnIn₂S₄ bilayer and half-unit-cell ZnIn₂S₄ monolayer have been fabricated using a one-step solvothermal method. Owing to the reduction of thickness, charge carriers would effectively migrate to surface within the shortened diffusion distance for improving the separation rate. Therefore, M-ZIS has an enhanced photocatalytic H₂ rate of 1.723 mmol/g/h under the visible-light irradiation, which is higher than that of B-ZIS. Further, the introduction of S vacancy in the ZnIn₂S₄ monolayer would capture the photo-generated electrons, thus extending the lifetime of photo-generated electron and hole. Due to the change of the electron structure, more charge carries

would participate in the photocatalytic activity and the holes can be rapidly consumed through the reaction with TEOA and water, resulting in an enhanced utilization rate of electrons. Therefore, M-ZIS-S exhibits an excellent photocatalytic H₂ production rate up to 13.478 mmol/g/h, improving by a factor of 7.8 by the introduction of S vacancy, much higher than the available values reported so far. Overall, the development of 2D materials monolayer with the vacancy is an effective strategy to improve photocatalytic H₂ production and provides a new insight into the optimization of photocatalysts.

Acknowledgements

The National Basic Research Program of China (2014CB931700) and State Key Laboratory of Optoelectronic Materials and Technologies supported this work.

Appendix A. Supplementary data

Supplementary material related to this article can be found, in the online version, at doi:<https://doi.org/10.1016/j.apcatb.2019.02.027>.

References

- [1] K. Maeda, K. Domen, Photocatalytic water splitting: recent progress and future challenges, *J. Phys. Chem. Lett.* 1 (18) (2010) 2655–2661.
- [2] S.J.A. Moniz, S.A. Shevlin, D.J. Martin, Z.-X. Guo, J. Tang, Visible-light driven heterojunction photocatalysts for water splitting—a critical review, *Energ. Environ. Sci.* 8 (3) (2015) 731–759.
- [3] Z.Y. Lin, L.H. Li, L.L. Yu, W.J. Li, G.W. Yang, Modifying photocatalysts for solar hydrogen evolution based on the electron behavior, *J. Mater. Chem. A* 5 (11) (2017) 5235–5259.
- [4] M. Zhou, X.W. Lou, Y. Xie, Two-dimensional nanosheets for photoelectrochemical water splitting: Possibilities and opportunities, *Nano Today* 8 (6) (2013) 598–618.
- [5] Z.C. Lai, Y. Chen, C.L. Tan, X. Zhang, H. Zhang, Self-Assembly of Two-Dimensional Nanosheets into One-Dimensional Nanostructures, *ChemUs* 1 (1) (2016) 59–77.
- [6] Z. Lei, W. You, M. Liu, G. Zhou, T. Takata, M. Hara, K. Domen, C. Li, Photocatalytic water reduction under visible light on a novel ZnIn₂S₄ catalyst synthesized by hydrothermal method, *Chem. Commun.* (2003) 17.
- [7] W.J. Li, Z.Y. Lin, G.W. Yang, A 2D self-assembled MoS₂/ZnIn₂S₄ heterostructure for efficient photocatalytic hydrogen evolution, *Nanoscale* 9 (46) (2017) 18290–18298.
- [8] B. Lin, H. Li, H. An, W. Hao, J. Wei, Y. Dai, C. Ma, G. Yang, Preparation of 2D/2D g-C₃N₄ nanosheet@ZnIn₂S₄ nanoleaf heterojunctions with well-designed high-speed charge transfer nanochannels towards high-efficiency photocatalytic hydrogen evolution, *Appl. Catal. B-Environ.* 220 (2018) 542–552.
- [9] B. Xu, P.L. He, H.L. Liu, P.P. Wang, G. Zhou, X. Wang, A 1D/2D Helical CdS/ZnIn₂S₄ Nano-Heterostructure, *Angew. Chem. Int. Ed.* 53 (9) (2014) 2339–2343.
- [10] W.J. Zhao, Z. Ghorannevis, K.K. Amara, J.R. Pang, M. Toh, X. Zhang, C. Kloc, P.H. Tan, G. Eda, Lattice dynamics in mono- and few-layer sheets of WS₂ and WSe₂, *Nanoscale* 5 (20) (2013) 9677–9683.
- [11] Y. Gao, W.C. Ren, T. Ma, Z.B. Liu, Y. Zhang, W.B. Liu, L.P. Ma, X.L. Ma, H.M. Cheng, Repeated and controlled growth of monolayer, bilayer and few-layer hexagonal boron nitride on Pt foils, *ACS Nano* 7 (6) (2013) 5199–5206.
- [12] A.L. Elias, N. Perea-Lopez, A. Castro-Beltran, A. Berkdemir, R.T. Lv, S.M. Feng, A.D. Long, T. Hayashi, Y.A. Kim, M. Endo, H.R. Gutierrez, N.R. Pradhan, L. Balicas, T.E. Mallouk, F. Lopez-Urías, H. Terrones, M. Terrones, Controlled synthesis and transfer of large-area WS₂ sheets: from single layer to few layers, *ACS Nano* 7 (6) (2013) 5235–5242.
- [13] R.T. Lv, J.A. Robinson, R.E. Schaak, D. Sun, Y.F. Sun, T.E. Mallouk, M. Terrones, Transition metal dichalcogenides and beyond: synthesis, properties, and applications of single- and few-layer nanosheets, *Accounts Chem. Res.* 48 (3) (2015) 897–897.
- [14] Y. Zhu, S. Murali, W. Cai, X. Li, J.W. Suk, J.R. Potts, R.S. Ruoff, Graphene and graphene oxide: synthesis, properties, and applications, *Adv. Mater.* 22 (35) (2010) 3906–3924.
- [15] X.S. Li, W.W. Cai, J.H. An, S. Kim, J. Nah, D.X. Yang, R. Piner, A. Velamakanni, I. Jung, E. Tutuc, S.K. Banerjee, L. Colombo, R.S. Ruoff, Large-area synthesis of high-quality and uniform graphene films on copper foils, *Science* 324 (5932) (2009) 1312–1314.
- [16] W. Cai, A.L. Moore, Y. Zhu, X. Li, S. Chen, L. Shi, R.S. Ruoff, Thermal transport in suspended and supported monolayer graphene grown by chemical vapor deposition, *Nano Lett.* 10 (5) (2010) 1645–1651.
- [17] D. Chen, X. Zhang, A.F. Lee, Synthetic strategies to nanostructured photocatalysts for CO₂ reduction to solar fuels and chemicals, *J. Mater. Chem. A* 3 (28) (2015) 14487–14516.
- [18] F. Lei, Y. Sun, K. Liu, S. Gao, L. Liang, B. Pan, Y. Xie, Oxygen vacancies confined in ultrathin indium oxide porous sheets for promoted visible-light water splitting, *J. Am. Chem. Soc.* 136 (19) (2014) 6826–6829.
- [19] Z. Fang, S. Weng, X. Ye, W. Feng, Z. Zheng, M. Lu, S. Lin, X. Fu, P. Liu, Defect Engineering and Phase Junction Architecture of Wide-Bandgap ZnS for Conflicting Visible Light Activity in Photocatalytic H₂ Evolution, *ACS Appl. Mater. Interfaces* 7 (25) (2015) 13915–13924.
- [20] Y. Lv, W. Yao, R. Zong, Y. Zhu, Fabrication of Wide-Range-Visible Photocatalyst Bi₂WO_{6-x} nanoplates via Surface Oxygen Vacancies, *Sci. Rep.* 6 (2016) 19347.
- [21] H. Tan, Z. Zhao, W.B. Zhu, E.N. Coker, B. Li, M. Zheng, W. Yu, H. Fan, Z. Sun, Oxygen vacancy enhanced photocatalytic activity of perovskite SrTiO₃, *ACS Appl. Mater. Interfaces* 6 (21) (2014) 19184–19190.
- [22] L. Yang, S. Wang, J. Mao, J. Deng, Q. Gao, Y. Tang, O.G. Schmidt, Hierarchical MoS₂/polyaniline nanowires with excellent electrochemical performance for lithium-ion batteries, *Adv. Mater.* 25 (8) (2013) 5807–5813.
- [23] J. Xie, H. Zhang, S. Li, R. Wang, X. Sun, M. Zhou, J. Zhou, X.W. Lou, Y. Xie, Defect-rich MoS₂ ultrathin nanosheets with additional active edge sites for enhanced electrocatalytic hydrogen evolution, *Adv. Mater.* 25 (40) (2013) 5807–5813.
- [24] Y. Xie, Y. Liu, H. Cui, W. Zhao, C. Yang, F. Huang, Facile solution-based fabrication of ZnIn₂S₄ nanocrystalline thin films and their photoelectrochemical properties, *J. Power Sources* 265 (2014) 62–66.
- [25] S. Shen, J. Chen, X. Wang, L. Zhao, L. Guo, Microwave-assisted hydrothermal synthesis of transition-metal doped ZnIn₂S₄ and its photocatalytic activity for hydrogen evolution under visible light, *J. Power Sources* 196 (23) (2011) 10112–10119.
- [26] L.Z. Iju, X.L. Wu, F. Gao, J.C. Shen, T.H. Li, P.K. Chu, Determination of surface oxygen vacancy position in SnO₂ nanocrystals by Raman spectroscopy, *Solid State Commun.* 151 (11) (2011) 811–814.
- [27] L. Wei, Y.J. Chen, Y.P. Lin, H.S. Wu, R.S. Yuan, Z.H. Li, MoS₂ as non-noble-metal co-catalyst for photocatalytic hydrogen evolution over hexagonal ZnIn₂S₄ under visible light irradiations, *Appl. Catal. B-Environ.* 144 (2014) 521–527.
- [28] A.Y. Lu, X.L. Yang, C.C. Tseng, S.X. Min, S.H. Lin, C.L. Hsu, H.N. Li, H.C. Idriss, J.L. Kuo, K.W. Huang, L.J. Li, High-Sulfur-Vacancy Amorphous Molybdenum Sulfide as a High Current Electrocatalyst in Hydrogen Evolution, *Small* 12 (40) (2016) 5530–5537.
- [29] X.Y. Zhang, Z. Zhao, W.W. Zhang, G.Q. Zhang, D. Qu, X. Miao, S.R. Sun, Z.C. Sun, Surface defects enhanced visible light photocatalytic H₂ production for Zn-Cd-S solid solution, *Small* 12 (6) (2016) 793–801.
- [30] S.Q. Zhang, X. Liu, C.B. Liu, S.L. Luo, L.L. Wang, T. Cai, Y.X. Zeng, J.L. Yuan, W.Y. Dong, Y. Pei, Y.T. Liu, MoS₂ Quantum Dot Growth Induced by S Vacancies in a ZnIn₂S₄ Monolayer: Atomic-Level Heterostructure for Photocatalytic Hydrogen Production, *ACS Nano* 12 (1) (2018) 751–758.
- [31] L. Li, L. Yu, Z. Lin, G. Yang, Reduced TiO₂-Graphene Oxide Heterostructure As Broad Spectrum-Driven Efficient Water-Splitting Photocatalysts, *ACS Appl. Mater. Interfaces* 8 (13) (2016) 8536–8545.
- [32] Y. Yin, J.C. Han, Y.M. Zhang, X.H. Zhang, P. Xu, Q. Yuan, L. Samad, X.J. Wang, Y. Wang, Z.H. Zhang, P. Zhang, X.Z. Cao, B. Song, S. Jin, Contributions of Phase, Sulfur Vacancies, and Edges to the Hydrogen Evolution Reaction Catalytic Activity of Porous Molybdenum Disulfide Nanosheets, *J. Am. Chem. Soc.* 138 (25) (2016) 7965–7972.
- [33] X.C. Jiao, Z.W. Chen, X.D. Li, Y.F. Sun, S. Gao, W.S. Yan, C.M. Wang, Q. Zhang, Y. Lin, Y. Luo, Y. Xie, Defect-mediated electron-hole separation in one-unit-Cell ZnIn₂S₄ layers for boosted solar-driven CO₂ reduction, *J. Am. Chem. Soc.* 139 (22) (2017) 7586–7594.
- [34] J. Wang, Y. Chen, W. Zhou, G. Tian, Y. Xiao, H. Fu, H. Fu, Cubic quantum dot/ hexagonal microsphere ZnIn₂S₄ heterophase junctions for exceptional visible-light-driven photocatalytic H₂ evolution, *J. Mater. Chem. A* 5 (18) (2017) 8451–8460.
- [35] B. Wang, X.H. Wang, L. Lu, C.G. Zhou, Z.Y. Xi, J.J. Wang, X.K. Ke, G.D. Sheng, S.C. Yan, Z.G. Zou, Oxygen-Vacancy-Activated CO₂Splitting over Amorphous Oxide Semiconductor Photocatalyst, *ACS Catal.* 8 (1) (2018) 516–525.
- [36] Z.Y. Zhang, J.D. Huang, Y.R. Fang, M.Y. Zhang, K.C. Liu, B. Dong, A Nonmetal Plasmonic Z-Scheme Photocatalyst with UV- to NIR-Driven Photocatalytic Protons Reduction, *Adv. Mater.* (18) (2017) 29.
- [37] X.T. Wang, C.H. Liow, A. Bisht, X.F. Liu, T.C. Sum, X.D. Chen, S.Z. Li, Engineering Interfacial Photo-Induced Charge Transfer Based on Nanobamboo Array Architecture for Efficient Solar-to-Chemical Energy Conversion, *Adv. Mater.* (13) (2015) 27.
- [38] X.L. Wang, Z.C. Feng, J.Y. Shi, G.Q. Jia, S.A. Shen, J. Zhou, C. Li, Trap states and carrier dynamics of TiO₂ studied by photoluminescence spectroscopy under weak excitation condition, *Phys. Chem. Chem. Phys.* 12 (26) (2010) 7083–7090.
- [39] J.H. Yang, D.G. Wang, H.X. Han, C. Li, Roles of Cocatalysts in Photocatalysis and Photoelectrocatalysis, *Accounts Chem. Res.* 46 (8) (2013) 1900–1909.
- [40] L. Li, Z. Deng, L. Yu, Z. Lin, W. Wang, G. Yang, Amorphous transitional metal borides as substitutes for Pt cocatalysts for photocatalytic water splitting, *Nano Energy* 27 (2016) 103–113.
- [41] X. Zhang, X. Xie, H. Wang, J. Zhang, B. Pan, Y. Xie, Enhanced photoresponsive ultrathin graphitic-phase C₃N₄ nanosheets for bioimaging, *J. Am. Chem. Soc.* 135 (1) (2013) 18–21.
- [42] W.L. Yang, L. Zhang, J.F. Xie, X.D. Zhang, Q.H. Liu, T. Yao, S.Q. Wei, Q. Zhang, Y. Xie, Enhanced Photoexcited Carrier Separation in Oxygen-Doped ZnIn₂S₄ Nanosheets for Hydrogen Evolution, *Angew. Chem. Int. Ed.* 55 (23) (2016) 6716–6720.
- [43] C. Du, D.H. Li, Q.Y. He, J.M. Liu, W. Li, G.N. He, Y.Z. Wang, Design and simple synthesis of composite Bi₁₂TiO₂₀/Bi₄Ti₃O₁₂ with a good photocatalytic quantum efficiency and high production of photo-generated hydroxyl radicals, *Phys. Chem. Chem. Phys.* 18 (38) (2016) 26530–26538.
- [44] Y. Nosaka, A.Y. Nosaka, Generation and Detection of Reactive Oxygen Species in Photocatalysis, *Chem. Rev.* 117 (17) (2017) 11302–11336.
- [45] Y. Jv, B.X. Li, R. Cao, Positively-charged gold nanoparticles as peroxidase mimic and their application in hydrogen peroxide and glucose detection, *Chem. Commun.* 46 (42) (2010) 8017–8019.
- [46] W. Sun, X.M. Ju, Y.Y. Zhang, X.H. Sun, G.J. Li, Z.F. Sun, Application of carboxyl functionalized graphene oxide as mimetic peroxidase for sensitive voltammetric detection of H₂O₂ with 3,3'-5,5'-tetramethylbenzidine, *Electrochim. Commun.* 26 (2013) 113–116.